LETTER

doi:10.1038/nature13962

Homo erectus at Trinil on Java used shells for tool production and engraving

Josephine C. A. Joordens[1,2], Francesco d'Errico[3,4], Frank P. Wesselingh[5], Stephen Munro[6,7], John de Vos[5], Jakob Wallinga[8,9], Christina Ankjærgaard[8,9], Tony Reimann[8,9], Jan R. Wijbrans[2], Klaudia F. Kuiper[2], Herman J. Mücher[1,10], Hélène Coqueugniot[3], Vincent Prié[11,12], Ineke Joosten[13], Bertil van Os[13], Anne S. Schulp[2,5,14], Michel Panuel[15,16], Victoria van der Haas[1], Wim Lustenhouwer[2], John J. G. Reijmer[2] & Wil Roebroeks[1]

The manufacture of geometric engravings is generally interpreted as indicative of modern cognition and behaviour[1]. Key questions in the debate on the origin of such behaviour are whether this innovation is restricted to *Homo sapiens*, and whether it has a uniquely African origin[1]. Here we report on a fossil freshwater shell assemblage from the *Hauptknochenschicht* ('main bone layer') of Trinil (Java, Indonesia), the type locality of *Homo erectus* discovered by Eugène Dubois in 1891 (refs 2 and 3). In the Dubois collection (in the Naturalis museum, Leiden, The Netherlands) we found evidence for freshwater shellfish consumption by hominins, one unambiguous shell tool, and a shell with a geometric engraving. We dated sediment contained in the shells with $^{40}Ar/^{39}Ar$ and luminescence dating methods, obtaining a maximum age of 0.54 ± 0.10 million years and a minimum age of 0.43 ± 0.05 million years. This implies that the Trinil *Hauptknochenschicht* is younger than previously estimated. Together, our data indicate that the engraving was made by *Homo erectus*, and that it is considerably older than the oldest geometric engravings described so far[4,5]. Although it is at present not possible to assess the function or meaning of the engraved shell, this discovery suggests that engraving abstract patterns was in the realm of Asian *Homo erectus* cognition and neuromotor control.

We analysed an assemblage of fossil freshwater mussel shells (*Pseudodon vondembuschianus trinilensis* Dubois 1908; Fig. 1) excavated in the 1890s from the Pleistocene *Hauptknochenschicht* at Trinil on Java (Extended Data Figs 1 and 2, Supplementary Tables 1 and 2). The Dubois collection from the Trinil *Hauptknochenschicht* contains 11 freshwater mollusc species and is numerically dominated by *Pseudodon* specimens[6]. The *Pseudodon* assemblage consists of 143 articulated shells, 23 single valves, and 24 fragments representing a minimum of 166 individuals (Supplementary Table 1). The sedimentary infillings of articulated shells indicate fluvial deposition under varying water levels and sediment loads, and include volcanic minerals transported along the river network draining volcanic uplands located south-southeast of Trinil[3,6,7]. The dominance of articulated shells in the assemblage and the micromorphology of the infillings suggest rapid filling and subsequent burial of the shells during deposition of the *Hauptknochenschicht* (Extended Data Fig. 1c–j).

The well preserved *Pseudodon* shell assemblage does not appear to represent burial of a natural, living population. First, 33% of the individuals display one or two characteristic holes in the shells at the location of the anterior adductor muscle (Fig. 1). Second, the assemblage contains only adult large-sized specimens (about 80–120 mm in length), while under normal conditions mussel populations comprise all age classes (Extended Data Fig. 1k). A possible excavators' bias in favour of large specimens does not explain this pattern, because the presence of much smaller shells, bones and shell fragments in the Dubois collection shows that fossil remains of all sizes were recovered and curated. Third, there is a large range in the length–width ratios of the *Pseudodon* shells, indicating that the assemblage includes specimens from several different environmental settings along a river. These observations indicate that the Trinil *Pseudodon* assemblage did not result from the burial of a living, local population, but was brought together by a size-selective agent collecting molluscs for consumption.

Most (79%) of the holes observed in the *Pseudodon* specimens correspond to the location of the anterior adductor muscle scar inside the shell; their diameter is about 5–10 mm. Potential mollusc-consuming agents at Trinil that could have produced the holes include otters (*Lutrogale* sp.), rats (*Rattus trinilensis*), monkeys (*Macaca* sp.), and hominins (*H. erectus*)[6]. However, the holes in the Trinil shells do not resemble the various types of damages caused by any of these non-hominin agents, nor those caused by birds, marine predatory snails, mantis shrimps, octopuses, and abiotic abrasion and dissolution processes (Extended Data Fig. 3a–f). Holes comparable to those of Trinil were made by pre-Hispanic modern human inhabitants of the Caribbean region in the gastropod *Lobatus gigas* (formerly known as *Strombus gigas*) (Extended Data Fig. 3g–i), with the purpose of detaching the adductor ligament[8].

To assess possible perforation techniques we conducted experiments with living freshwater mussels of the same family, comparable in size and shell thickness to the extinct Trinil *Pseudodon* (Extended Data Fig. 3j–m). A pointed object such as a shark tooth—several of which were present in the Trinil *Hauptknochenschicht*—(Extended Data Fig. 3n–s), employed with a rotating motion into the living shell at the location of the anterior adductor muscle, produces a hole similar in size and morphology to the holes from Trinil (Fig. 1d). As soon as the shell is pierced and the muscle has been damaged by the tool tip, the animal loses control of the muscle, the valves part and the shell can be opened without breakage (Supplementary Video 1). Our experiments indicate that a high level of dexterity and knowledge of mollusc anatomy is required to open shells in this way. The absence of holes similar to those at Trinil in natural shell assemblages, the difference between the holes observed in the Trinil assemblage and those produced by non-human animals and abiotic factors, and the similarity between our experimental holes, human-made *Lobatus* holes and Trinil holes all suggest that *H. erectus* was the

[1]Faculty of Archaeology, Leiden University, PO Box 9515, 2300RA, Leiden, The Netherlands. [2]Faculty of Earth and Life Sciences, VU University Amsterdam, De Boelelaan 1085, 1081HV, Amsterdam, The Netherlands. [3]Université de Bordeaux, CNRS UMR 5199, Allée Geoffroy Saint-Hilaire, 33615 Pessac, France. [4]Institute of Archaeology, History, Cultural Studies and Religion, University of Bergen, Øysteinsgate 3, PO Box 7805, Bergen, Norway. [5]Naturalis Biodiversity Center, Darwinweg 2, PO Box 9517, 2300RA, Leiden, The Netherlands. [6]School of Archaeology and Anthropology, Australian National University, Australian Capital Territory, 0200 Canberra, Australia. [7]National Museum of Australia, Australian Capital Territory 2601, Canberra, Australia. [8]Wageningen University, Soil Geography and Landscape Group & Netherlands Centre for Luminescence Dating, PO Box 47, 6700AA, Wageningen, The Netherlands. [9]Delft University of Technology, Faculty of Applied Sciences, Mekelweg 15, 2629JB, Delft, The Netherlands. [10]Prinses Beatrixsingel 21, 6301VK, Valkenburg, The Netherlands. [11]Muséum National d'Histoire Naturelle, UMR 7205, Institut de Systématique, Evolution, Biodiversité, CP51, 55 Rue Buffon, 75005 Paris, France. [12]Biotope Recherche et Développement, 22 Boulevard Maréchal Foch, 34140 Mèze, France. [13]Cultural Heritage Agency of the Netherlands, PO Box 1600, 3800BP, Amersfoort, The Netherlands. [14]Natuurhistorisch Museum Maastricht, De Bosquetplein 7, 6211KJ, Maastricht, The Netherlands. [15]Faculté de Médecine, Université d'Aix-Marseille, EFS, CNRS UMR 7268, Boulevard Pierre Dramard, 13344 Marseille, France. [16]Department of Medical Imaging Hôpital Nord, Assistance Publique – Hôpitaux de Marseille, Chemin de Bourrellys, 13915 Marseille, France.

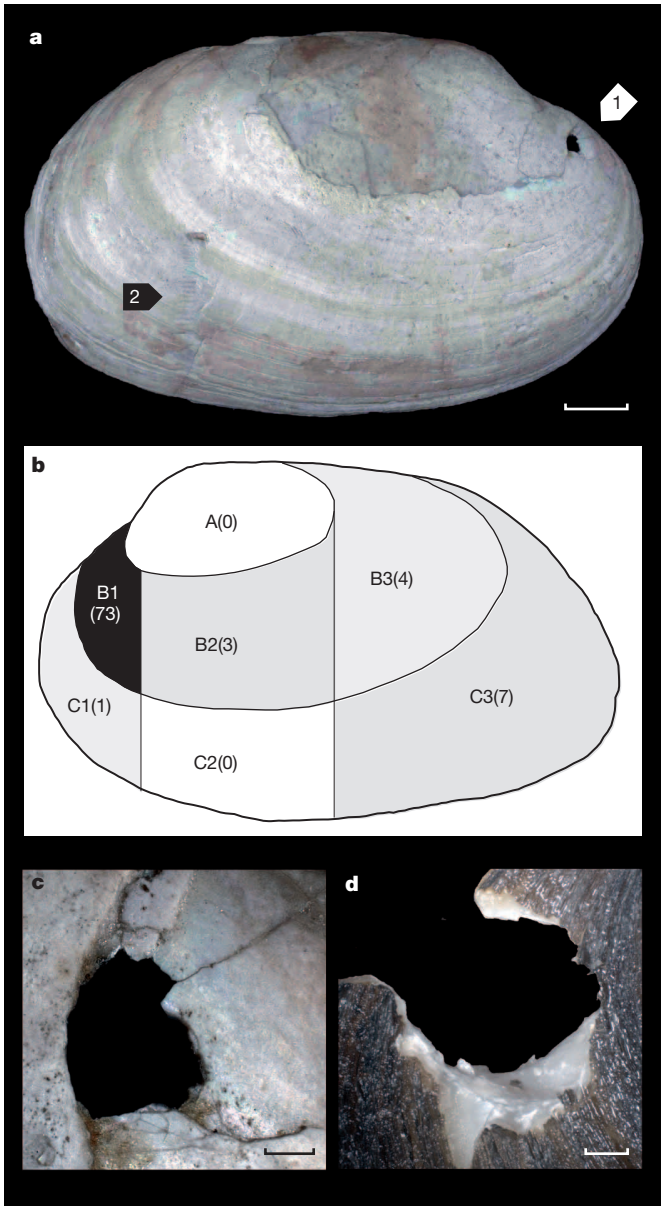

Figure 1 | Holes in unionoid shells. **a**, Example of a characteristic hole in fossil *Pseudodon* DUB 9723-bL from Trinil. Shown are: (1) a hole at the location of the anterior adductor muscle, (2) an impact pit with an associated scoring mark (Supplementary Information section 8). **b**, Incidence of holes in different areas (A–C3) of the Trinil *Pseudodon* shells (both left and right valves). **c**, Detail of hole from Fig. 1a. **d**, Detail of experimental hole in modern *Potamida littoralis* (Extended Data Fig. 3). Scale bars, 1 cm in **a**; 1 mm in **c** and **d**.

responsible agent. We conclude that the Trinil *Pseudodon* assemblage reflects the remains of shellfish collecting and processing by *H. erectus* along the banks of a river.

One of the *Pseudodon* shell valves from Trinil, specimen DUB5234-dL, shows signs of modification by retouch (Extended Data Fig. 4). The ventral margin features contiguous flake scars, which expose the nacreous layer between the ventral margin and the pallial line. The nacreous edge is smoothed and polished, suggesting its use as a tool for cutting or scraping. Indurated sediment and micro-concretions adhering to concavities produced by the retouch testify to the antiquity of the modification. Shallow striations run parallel to the retouched edge and traces of roots or fungi are present inside and across the striations, demonstrating that they pre-date weathering of the shell before or after burial. The striations most probably result from contact of the inner shell surface with hard materials while using the tool. Our results support the hypothesis[9] that shell tools were part of the cultural adaptations of *Homo erectus* on Java.

One of the *Pseudodon* shells, specimen DUB1006-fL, displays a geometric pattern of grooves on the central part of the left valve (Fig. 2). The pattern consists, from posterior to anterior, of a zigzag line with three sharp turns producing an 'M' shape, a set of more superficial parallel lines, and a zigzag with two turns producing a mirrored 'N' shape. Our study of the morphology of the zigzags, internal morphology of the grooves, and differential roughness of the surrounding shell area demonstrates that the grooves were deliberately engraved and pre-date shell burial and weathering (Extended Data Fig. 5). Comparison with experimentally made grooves on a fossil *Pseudodon* fragment reveals that the Trinil grooves are most similar to the experimental grooves made with a shark tooth; these experimental grooves also feature an asymmetrical cross-section with one ridge and no striations inside the groove (Extended Data Fig. 6). We conclude that the grooves in DUB1006-fL were made with a pointed hard object, such as a fossil or a fresh shark tooth, present in the Trinil palaeoenvironment. The engraving was probably made on a fresh shell specimen still retaining its brown periostracum, which would have produced a striking pattern of white lines on a dark 'canvas'. Experimental engraving of a fresh unionid shell revealed that considerable force is needed to penetrate the periostracum and the underlying prismatic aragonite layers. If the engraving of DUB1006-fL only superficially affected the aragonite layers, lines may easily have disappeared through weathering after loss of the outer organic layer. In addition, substantial manual control is required to produce straight deep lines and sharp turns as on DUB1006-fL. There are no gaps between the lines at the turning points, suggesting that attention was paid to make a consistent pattern. Together with the morphological similarity of all grooves, this indicates that a single individual made the whole pattern in a single session with the same tool.

Age estimates for the Trinil *Hauptknochenschicht* vary from the Early to the early Middle Pleistocene stages, usually based on correlation of the Trinil *Hauptknochenschicht* with the *Grenzbank* layer at Sangiran on Java[10,11]. However, such lithological correlations should be tested with direct chronological methods[12]. The presence of sediment-infilled *Pseudodon* shells enabled us to obtain direct $^{40}Ar/^{39}Ar$ and luminescence

Table 1 | Luminescence ages of *Pseudodon* shell infill samples

Sample code	*n*	Minimum equivalent dose (Gy)	Minimum palaeodose (Gy)			Total dose rate (Gy per kyr)	Minimum age (kyr)		
			± total error	± systematic uncertainty	± random uncertainty		± total error	± systematic uncertainty	± random uncertainty
DUB9735	9	525 ± 55	495 ± 57	18	54	1.09 ± 0.13	454 ± 75	54	51
DUB9736	6	507 ± 65	477 ± 66	18	64	1.21 ± 0.08	394 ± 61	29	54
DUB1006-f(I)	7	519 ±88	489 ± 89	18	87	1.15 ± 0.12	426 ± 89	45	76
DUB1006-f(II)	14	582 ±84	552 ± 85	19	83	1.19 ± 0.12	465 ± 87	50	71
DUB1006-e	19	492 ±43	462 ± 46	18	42	1.13 ± 0.12	408 ± 58	44	38
Average value							429 ± 46	44	13

Gy, absorbed radiation dose in grays; kyr, thousand years. The minimum equivalent dose is based on the sample average $2D_0$ values for pIRIR[20] dose–response curves of individual aliquots, where D_0 is a parameter indicating the onset of saturation in a saturating exponential plus linear fit of the data, and pIRIR is the measurement protocol used (see Methods section 'Luminescence dating'). The minimum palaeodose is obtained by subtracting an estimated residual dose at the time of deposition (30 ± 15 Gy; refs 20 and [21]) from the minimum equivalent dose. Uncertainties are provided at the 1σ level. Systematic uncertainties are those shared by all samples. The random uncertainty on the average value is based on the 1σ standard error on the mean of the minimum ages. Total uncertainties contain both systematic and random uncertainties. See Extended Data Fig. 9.

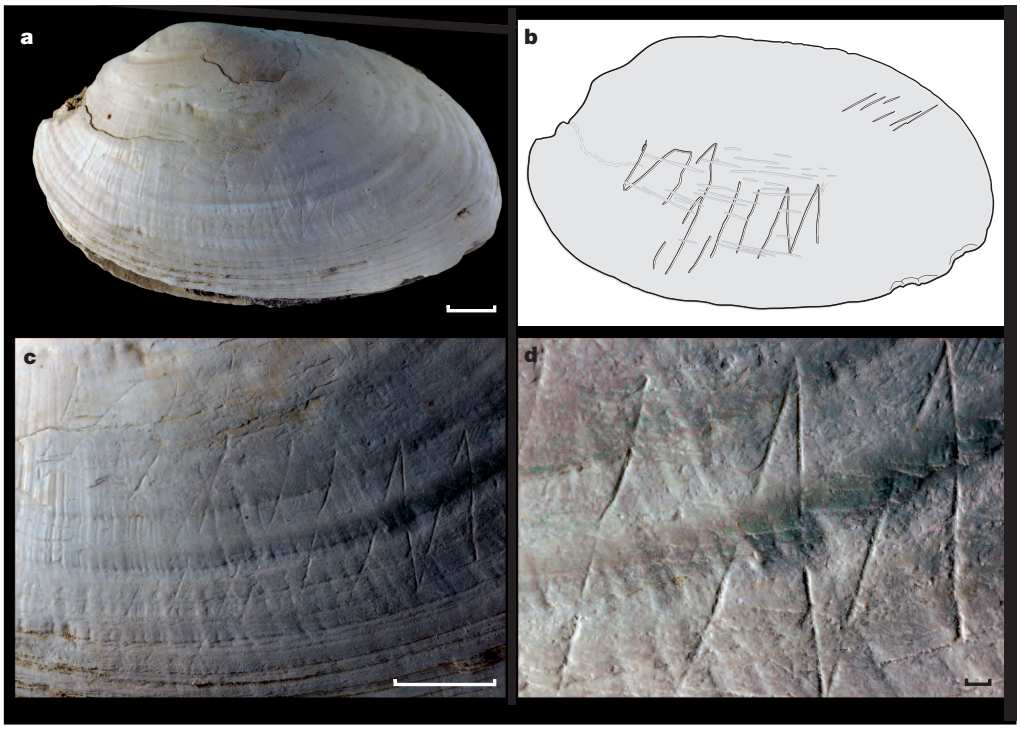

Figure 2 | The geometric pattern on *Pseudodon* DUB1006-fL. **a**, Overview. **b**, Schematic representation. **c**, Detail of main engraving area. **d**, Detail of posterior engravings. Scale bars, 1 cm in **a** and **c**; 1 mm in **d**. See also Extended Data Figs 5 and 6.

dating evidence for the age of the shells from the Trinil *Hauptknochenschicht*. The $^{40}Ar/^{39}Ar$ approach provides a maximum age: the sediment infill cannot be older than the youngest volcanic event being dated, but can be younger. Luminescence dating was performed to obtain a burial (minimum) age for the sediments inside the shells. The $^{40}Ar/^{39}Ar$ analysis of hornblende minerals picked from shell infills yielded, for each shell, three age groups of 1.65 ± 0.04 million years (Myr), 1.12 ± 0.04 Myr and 0.64 ± 0.06 Myr, respectively, reflecting three periods of volcanic activity (Extended Data Fig. 7 and 8, and Supplementary Table 5). For the youngest hornblende age group, which is crucial for defining the maximum age of the *Hauptknochenschicht* shells, the corresponding isochron age of 0.54 ± 0.10 Myr is the best representation of the true age of this group. Luminescence studies on feldspar from the sediment fill of four shells (including the engraved shell DUB1006-fL) provided an average minimum age of 0.43 ± 0.05 Myr (Table 1, Extended Data Fig. 9 and Supplementary Table 6). Hence the maximum and minimum age of the shells, including 1σ uncertainties, situates them in the middle part of the Middle Pleistocene. These are the first direct ages for sediments from the Trinil *Hauptknochenschicht*, suggesting it to be younger than has been estimated thus far. The minimum age unequivocally indicates that *H. erectus* and not *H. sapiens* must have made the shell modifications. Our results highlight that the sediments of the *Hauptknochenschicht* contain volcanic material from different eruptions, as expected on Java where run-off, floods and lahars from the volcanic uplands bring a mix of volcanic material of different ages into the lowlands. These findings underline that it is crucial for future chronological studies on Java to use additional dating methods to constrain $^{40}Ar/^{39}Ar$ ages[13,14] and to critically evaluate previously reported $^{40}Ar/^{39}Ar$ ages for the first appearance of *H. erectus* on Java[15].

The combined evidence for high-dexterity opening of shells, use of shell as a raw material to make tools, and engraving of an abstract pattern on a shell with a minimum age of 0.43 ± 0.05 Myr indicates that *H. erectus* was the agent responsible for the exploitation of freshwater mussels at Trinil described here. The inclusion of mussels in the diet of *H. erectus* is not surprising, as predation on aquatic molluscs is observed for many terrestrial mammals, including primates[6,16,17]. The reported use of shells as raw material for tool production is the earliest known in the history of hominin technology. It may explain the absence of unambiguous stone artefacts in the Early and Middle Pleistocene of Java[9,18], possibly the result of poor local availability of lithic raw material, as also suggested for the much younger (about 110,000 years old) Neanderthal shell tools from Italy and Greece[19]. Our discovery of an engraving on shell substrate is unexpected, because the earliest previously known undisputable engravings are at least 300,000 years younger[4,5] (Extended Data Fig. 10). We predict that it is only a matter of time before comparable evidence is discovered, filling the gap between this early case of shellfish exploitation, shell tool use and engraving, and its later counterparts.

Online Content Methods, along with any additional Extended Data display items and Source Data, are available in the online version of the paper; references unique to these sections appear only in the online paper.

Received 22 May; accepted 13 October 2014.
Published online 3 December 2014.

1. d'Errico, F. & Stringer, C. B. Evolution, revolution or saltation scenario for the emergence of modern cultures? *Phil. Trans. R. Soc. B* **366,** 1060–1069 (2011).
2. Dubois, E. *Pithecanthropus Erectus, Eine Menschenähnliche Übergangsform aus Java* (Landesdruckerei, 1894).
3. Dubois, E. Das geologische Alter der Kendeng- oder Trinil-fauna. *Tijdschr. Kon. Ned. Aardr. Gen.* **25,** 1235–1270 (1908).
4. Henshilwood, C. S., d'Errico, F. & Watts, I. Engraved ochres from the Middle Stone Age levels at Blombos Cave, South Africa. *J. Hum. Evol.* **57,** 27–47 (2009).
5. d'Errico, F., García Moreno, R. & Rifkin, R. F. Technological, elemental and colorimetric analysis of an engraved ochre fragment from the Middle Stone Age levels of Klasies River Cave 1, South Africa. *J. Archaeol. Sci.* **39,** 942–952 (2012).
6. Joordens, J. C. A., Wesselingh, F. P., de Vos, J., Vonhof, H. B. & Kroon, D. Relevance of aquatic environments for hominins: a case study from Trinil (Java, Indonesia). *J. Hum. Evol.* **57,** 656–671 (2009).
7. Huffman, O. F. *et al.* Volcanic mountains, river valleys and sea coasts—the paleoenvironment of *Homo erectus* in eastern Java (Indonesia). *Quat. Int. Spec. Issue XVIII INQUA Congr. (21st–27th July, 2011, Bern)* (eds Schlüchter C. & Nietlispach, J.) **279–280,** 210 (2012).
8. Antczak, A. & Mackowiak de Antczak, M. M. in *Caribbean Marine Biodiversity: The Known and Unknown* (eds P. Miloslavich & E. Klein) 213–245 (DEStech, 2005).
9. Choi, K. & Driwantoro, D. Shell tool use by early members of *Homo erectus* in Sangiran, central Java, Indonesia: cut mark evidence. *J. Archaeol. Sci.* **34,** 48–58 (2007).

10. Dennell, R. *The Palaeolithic Settlement of Asia* (Cambridge Univ. Press, 2009).
11. Larick, R. *et al.* Early Pleistocene $^{40}Ar/^{39}Ar$ ages for Bapang Formation hominins, Central Jawa, Indonesia. *Proc. Natl Acad. Sci. USA* **98,** 4866–4871 (2001).
12. Joordens, J. C. A. *et al.* Improved age control on early *Homo* fossils from the upper Burgi Member at Koobi Fora, Kenya. *J. Hum. Evol.* **65,** 731–745 (2013).
13. Hyodo, M. *et al.* High-resolution record of the Matuyama–Brunhes transition constrains the age of Javanese *Homo erectus* in the Sangiran dome, Indonesia. *Proc. Natl Acad. Sci. USA* **108,** 19563–19568 (2011).
14. Indriati, E. *et al.* The age of the 20 Meter Solo River Terrace, Java, Indonesia and the survival of *Homo erectus* in Asia. *PLoS ONE* **6,** e21562 (2011).
15. Huffman, O. F. *et al.* Relocation of the 1936 Mojokerto skull discovery site near Perning, East Java. *J. Hum. Evol.* **50,** 431–451 (2006).
16. Carlton, J. T. & Hodder, J. Maritime mammals: terrestrial mammals as consumers in marine intertidal communities. *Mar. Ecol. Prog. Ser.* **256,** 271–286 (2003).
17. Gumert, M. D. & Malaivijitnond, S. Marine prey processed with stone tools by burmese long-tailed macaques (*Macaca fascicularis aurea*) in intertidal habitats. *Am. J. Phys. Anthropol.* **149,** 447–457 (2012).
18. Stone, R. Java Man's first tools. *Science* **312,** 361 (2006).
19. Douka, K. & Spinapolice, E. Neanderthal shell tool production: evidence from Middle Palaeolithic Italy and Greece. *J. World Prehist.* **25,** 45–79 (2012).
20. Buylaert, J. P. *et al.* A robust feldspar luminescence dating method for Middle and Late Pleistocene sediments. *Boreas* **41,** 435–451 (2012).
21. Alexanderson, H. & Murray, A. S. Luminescence signals from modern sediments in a glaciated bay, NW Svalbard. *Quat. Geochronol.* **10,** 250–256 (2012).

Supplementary Information is available in the online version of the paper.

Acknowledgements We thank colleagues O. F. Huffman, P. Albers, R. Dennell, M. Martinón-Torres, G. Cadée, O. Dutour, K. M. Cohen, P. de Boer, A. van Gijn, C. Hofman, Y. Lammers-Keijsers, A. C. Sorensen, W. Renema, R. Moolenbeek, R. van Zelst, C. A. Johns, A. J. Versendaal, E. Voskuilen, T. G. van Meerten, R. van Elsas, H. Vonhof, S. Kars, W. Koot, P. Bouchet, V. Héros, J. W. Dogger, L. Dekkers, B. Dutailly, G. Devilder and J. Porck. J.C.A.J., W.R. and T.R. acknowledge financial support from the Netherlands Organization for Scientific Research NWO (Open Programme Grant to J.C.A.J., Spinoza Grant 28-548 to W.R. and Rubicon Grant 825.11.03 to T.R.). F.d'E. acknowledges financial support from the European Research Council (FP7/2007/2013, TRACSYMBOLS 249587), and C.A. acknowledges financial support from the STW Technology Foundation (STW.10502).

Author Contributions J.C.A.J., F.d'E., F.P.W. and W.R. conceived the study. J.C.A.J., F.d'E., F.P.W. and S.M. analysed the shell assemblage. S.M. discovered the engraving. F.d'E. and J.C.A.J. studied the tool and the engraving, assisted by W.L. I.J. did the SEM imaging. J.W., C.A. and T.R. carried out the luminescence dating. J.R.W. and K.F.K. carried out the $^{40}Ar/^{39}Ar$ dating assisted by V.v.d.H. H.J.M. carried out the micromorphological analysis. V.P. and J.C.A.J. conducted the shell opening experiments. B.v.O., A.S.S. and J.C.A.J. performed the XRF analysis. M.P. did the CT scanning, H.C. carried out the 3D analysis and directed the video. J.C.A.J., F.d'E., F.P.W. and W.R. wrote the paper, with contributions by all other co-authors.

Author Information Reprints and permissions information is available at www.nature.com/reprints. The authors declare no competing financial interests. Readers are welcome to comment on the online version of the paper. Correspondence and requests for materials should be addressed to J.C.A.J. (j.c.a.joordens@arch.leidenuniv.nl).

METHODS

Description of the *Pseudodon* shell assemblage. All complete *Pseudodon* shell specimens were measured with a digital caliper. Length was measured along the longest axis of the shell; the height is the maximum length perpendicular to the long axis. Each valve was given a unique number (for example, DUB5234b-L) consisting of the Dubois catalogue number assigned by Dubois and his assistant Bernsen to a "field lot" containing several specimens[22], followed by a lower-case letter for each specimen from that box, and a hyphen plus an L or R indicating a left or right valve, respectively. These two letters were added during this study to enable identification of each shell specimen in a field lot. We also recorded whether shells consisted of single or paired, still connected valves, and in the latter case, whether the valves were closed or partially open. The valve area was divided into seven zones (A-C3, see Fig. 1b), and the presence of breakage, etching, dissolution pits, desquamation, abrasion, holes and grooves was recorded for each zone.

Micromorphological sediment analysis. To obtain further information on the depositional environment of Trinil *Hauptknochenschicht* and the depositional history of the *Pseudodon* shells, we conducted micromorphological sediment analysis on two *Pseudodon* shell infillings. Thin sections were produced from shell infillings (DUB9717-b and DUB9735) by making two vertical cross-sections along both the length and the width of the infillings, using established methods[23,24]. The thin sections were subsequently described following established terminology[25]. The infilling is obliquely oriented with respect to the shell axis.

Comparison of *Pseudon* assemblage to recent shells. Length and height data of the fossil *Pseudodon vondembuschianus trinilensis* Dubois 1908 shells from Trinil were compared with those measured on recent *Pseudodon vondembuschianus* Lea 1840, collected by several researchers on Java. These shells are part of the Mollusca collections housed at the natural history museum Naturalis in Leiden, The Netherlands. The collectors are: W. C. van Heurn, who in 1935 collected near Surabaya at three different locations named 1a ($n = 24$ specimens), 1b ($n = 40$) and 1c ($n = 34$); Heysmann ($n = 20$), and Groen ($n = 12$) who both collected on Java (no further indication of location). In addition, we included in the comparison the length–height data that we obtained from measuring a unionid freshwater bivalve population (*Unio crassus* Philipson 1788; $n = 50$) sampled by L. Pascal from the Seine River (Neuilly, France) in 1849 (ref. 26). This collection is housed at the Muséum National d'Histoire Naturelle in Paris, France. All measurements were done with a digital caliper. Length was measured along the longest axis of the shell; the height is the maximum length perpendicular to the long axis.

X-ray fluorescence analyses. To assess the stratigraphical integrity of the Trinil *Hauptknochenschicht* we conducted multiple X-ray fluorescence (XRF) analyses on hominin and non-hominin fossil bones from the Trinil *Hauptknochenschicht* and from the nearby site Kedung Brubus (see Extended Data Fig. 1a), and on a modern human femur present in the Dubois Collection. This non-destructive analysis method is the only chemical analysis that we could apply to the bones, since any method involving the drilling of powder out of the fossil bone, or transport of the fossil bones outside Naturalis, was not allowed. Data were acquired using a hand-held portable XRF device, a Thermo Scientific Niton XL3t with GOLDD detector equipped with a silver anode operating at a maximum of 50 kV and 40 mA. The device is well suited for the measurement of up to 25 elements simultaneously in the analytical range between S (atomic number 16) and U (atomic number 92) as well as light elements (Mg, Al, Si, P and Cl). Lighter elements such as F (atomic number 9) cannot be measured with this device. The device is factory-calibrated and further soil reference material was measured for external standardization. All analyses were performed in bulk mode ('mining mode'). All fossil bones were measured directly by hand, with several (from four up to seven) measurements per fossil, at different spots on the bone where the surface was flat. Each measurement lasted 110 s, using four different energy settings for light (Al, Si, P, S, Cl), low (Ca, K, Sc, Ti), main (K-lines from V until Ag and L-lines from Au until Pb) and high Z elements (Ag until Au). Yttrium (Y) contents are not reported by the software, so raw counts are extracted from the Y Kα1 line (14.96 keV) and corrected for the Ca yield. This peak overlaps with the Rb Kβ1 line, but Rb contents as derived from the Kα1 line are too low to have a significant contribution to the Y counts.

Experimental opening of living bivalve molluscs. To assess how the holes observed in fossil *Pseudodon* shells could have been made, we conducted opening experiments with living freshwater unionid mussels that are comparable in size, shell thickness and structure to the extinct *Pseudodon* species from Trinil. The shell matrix of living unionoid shells consists of a thick periostracum overlying aragonitic layers and contains organic material, which provides both strength and elasticity. After death of the mollusc, the shell material becomes more rigid and brittle owing to degradation of organic matter during the drying and/or fossilization process. We therefore performed these experiments on living instead of recently dead or fossil mussels. We used one living *Potamida littoralis* Lamarck 1801 from Nouâtres, Vienne River (France), and one *Unio mancus turtonii* Payraudeau 1826 from the Tavignanu River, Corsica (France). The two specimens were kept alive in an aquarium until the time of the experiments. Since our experimental research on the engraved shell (see below) had indicated that a shark tooth was the most likely tool used to make the engraving, we used a shark tooth as a tool to experimentally perforate live unionid shells.

Computed tomography (CT) scans of living bivalve molluscs. Before the opening experiments (see above), the two live mollusc specimens were taken to the Department of Medical Imaging of Marseille Hôpital Nord, in order to obtain CT scans, used as the basis for a video animation on opening the shells (Supplementary Video 1). The specimens were scanned using a Siemens Sensation Cardiac 64 scanner, yielding a 512 × 512 pixel matrix. Acquisition specifications were: slice thickness (in mm) = 0.6; space between slices (in mm) = 0.4; source peak voltage (in kV) = 100; current (in mA) = 220; generator power (in kW) = 22. The CT scans were processed with TIVMI (Treatment and Increased Vision for Medical Imaging) software developed by Bruno Dutailly. This program (http://www.pacea.u-bordeaux1.fr/TIVMI/) was designed for morphometrics and anthropological research. TIVMI offers an automatic computation of the HMH algorithm[27], which helps to identify, independently of the user, the exact interface between two different tissues or materials. In three dimensions, the HMH is computed at each voxel for extracting a reproducible and reliable surface[28]. Therefore, three-dimensional surfaces of the shell and mantle were automatically extracted using this HMH three-dimensional algorithm. The shell is represented as transparent in order to visualize the muscle attachment of the anterior adductor muscle.

Analysis of modifications on shells. Two *Pseudodon* shell specimens (DUB5234-dL and DUB9723-bL) were examined and photographed at magnifications between 4× and 40× with a motorised Leica Z6 APOA microscope equipped with a DFC420 digital camera and Leica Application Suite (LAS) software, including the Multifocus module. With this microscope, once digital images have been acquired at different heights, adapted algorithms combine them into a single sharp composite image that significantly extends the depth of field. Interpretation of recorded modifications is based on known criteria to identify taphonomic damage on freshwater shells[29–31] and experimental shell manufacture and use[11,19,29,30,32–36].

Analysis of the engraved shell. The *Pseudodon* specimen DUB1006-fL was photographed under incident light oriented in different directions and angles. The zigzag pattern and the other engraved lines detected on the specimen surface were examined with the same equipment and at the same magnifications as described for the specimens bearing evidence of being modified and used as tools (see above). Digitized images were imported into Adobe Illustrator to produce a tracing of the engravings, which was subsequently verified by comparing it to the original. Only the lines that were unambiguously verified as having been engraved were included in the tracing. In addition, engraved areas on DUB1006-fL as well as experimental engravings (see below) were analysed with a JEOL JSM-5910LV variable pressure scanning electron microscope (SEM) housed at the Cultural Heritage Agency of the Netherlands in Amsterdam (The Netherlands). The SEM was equipped with an Energy Dispersive X-ray Spectroscopy detector (Silicon Drift Detector, Noran System Seven software, Thermo Fisher Scientific) and the analysis was conducted at a voltage of 20 kV.

Selected areas of grooves and shell surface of DUB1006-fL, as well as experimentally made grooves (see below) were captured using an Alicona 3D Infinite Focus imaging microscope housed at ST Instruments, Groot-Ammers, The Netherlands. This equipment produces an accurate true-colour three-dimensional rendering of a surface with a vertical resolution of up to 10 nm (ref. 37). We scanned portions of grooves, intersections, and unmodified spots close to the groves in convex and concave areas of the shell surface architecture. Acquired data were used to produce and compare surfaces topographic rendering, grooves sections, and calculate three-dimensional roughness parameters (Sk, Sa, Sq, Sp, Sv, Sz, Ssk, Sku) at high vertical resolution. The engraving techniques used, the type of tool involved, the direction of the lines and the identification of lines produced in a single session by the same tool were established on the basis of known experimental criteria[38,39], comparison with published early engravings[40–42], and comparison with experimental markings conducted in the framework of this study. The latter consist of a series of linear engravings on a fragment of a fossil *Pseudodon* shell and on fresh unionid shell made with a flint point, a steel scalpel, and a shark tooth crown tip.

$^{40}Ar/^{39}Ar$ dating. Much of the coarser detritus found in the fossil *Pseudodon* shells during thin-section analysis (see above) was identified as being of volcanic origin, hence $^{40}Ar/^{39}Ar$ dating of this detritus was used to shed light on the age of the shells. An accurate $^{40}Ar/^{39}Ar$ date of this material will reflect a maximum age for the shell bed if the infill of the shells occurred simultaneously with deposition of this bed. The youngest component of the (potentially reworked) volcanic material then provides a maximum age of the shell bed. We sampled loose sediment from one of the Naturalis boxes holding *Pseudodon* shells (sample Trinil-1) and selected two shells with a detrital infilling: DUB9721-bR (sample Trinil-2) and DUB9714-bR (sample Trinil-3). The latter shell has a characteristic hole at the location of the anterior adductor muscle, indicating hominin modification (see main text). Selection

of the shells was based on the amount and coarseness of the detritus embedded in the shell.

Mineral separation of the detritus from the three samples took place at the VU University Mineral Separation Laboratory in Amsterdam. The detritus was pulverized, sieved (rejecting the >500 μm fraction) and subjected to heavy liquid mineral separation using diiodomethane with a density of 2.54 g ml^{-1} in a specially designed centrifuge. After liquid separation, electromagnetic separation (with a Frantz magnet) was applied to separate magnetic from non-magnetic minerals. Finally, discrete fractions of glass shards, feldspar and hornblende minerals were obtained by handpicking using a microscope. After handpicking, samples were packed in Al-foil envelopes and stacked in an Al-foil cylinder with Fish Canyon Tuff sanidines (28.198 Myr; ref. 43; standard age calculated with decay constants from ref. 44) as neutron flux monitors (standards) between each group of four or five packages containing unknowns. The samples were irradiated in the RODEO, a rotating (at 1 Hz) facility next to the reactor pool fitted with a Cd inner tube to shield the samples for excessive dosage of thermal neutrons at the High Flux reactor in Petten, The Netherlands. The experiments with the glass shards and the feldspar fractions (irradiation batch VU90) were irradiated for 10 h, and the hornblende (irradiation batch VU94) was irradiated for 1 h. To correct for interfering isotope reactions occurring during irradiation we used: $(^{40}Ar/^{39}Ar)_K$: 0.00134 ± 0.000787, $(^{39}Ar/^{37}Ar)_{Ca}$: 0.000733 ± 0.000035, $(^{36}Ar/^{37}Ar)_{Ca}$: 0.000265 ± 0.000008. For the $(^{40}Ar/^{36}Ar)_{Air}$ correction, the value of Lee and colleagues[45] (298.56 ± 0.18) was used.

As the individual grains were too small to allow a single grain fusion approach, we loaded small amounts (up to 10–15 grains) in a Cu tray with holes of 2 mm diameter and 3 mm depth. The samples were subjected to an overnight pre-bake-out stage in a vacuum house fitted with a Pyrex glass window, where the sample house was heated with a heating element to 150 °C, and in addition, the samples received direct heat from a 500-W heating lamp. Subsequently, the sample tray was loaded into the mass spectrometer sample house, fitted with a double vacuum multi-spectral ZnS CO_2 laser window. To bring the background argon down further, individual sample splits were pre-heated with a defocused laser beam to about 400 °C (using a 0–50-W continuous-wave maximum Synrad 48-5 CO_2 laser). The experiments were run in an automated run mode on a MAP 215-50 noble-gas mass spectrometer, equipped with a sample purification system that uses a three-stage clean up using a filament-heated SAES Zr-Al NP10 unit, a resistance-heated SAES ST172 Fe-V-Zr, and an Inconel tube filled with activated Ti-sponge getter. The MAP215-50 instrument is fitted with a Balzers SEM216 dynode secondary electron multiplier detector run in current mode. The relative gain with respect to the Faraday cup channel operated with a 10^{11}-ohm resistor amplifier was 5, 50 or 500, chosen automatically from the beam intensity of the sample ^{40}Ar beam during initial peak centring. Blanks were always run with the SEM detector gain at 500. Data collection used a protocol where twelve cycles through the argon spectrum were performed from 40 to 35.5 at half-mass-unit intervals, collecting 16 samples of 1-s integration time for all argon peaks, except ^{37}Ar where 12 1-s samples were used. Base lines were measured at the half-masses, using 6 1-s samples per analysis. Raw peak intensity data was regressed using ArArCalc-2.5 software[46]. During these measurements, sample-to-blank peak intensities both on $m/e = 40$ and $m/e = 36$ were better than about 100 (blank $m/e = 40$: 0.045–0.070 V, $m/e = 39$: 0–0.0007 V, $m/e = 38$: 0.00005–0.00013 V; $m/e = 37$: 0.0003–0.0020 V, and $m/e = 36$: 0.0003–0.0011 V, with a sensitivity of 3.3×10^{-15} moles of argon per volt (V).). The decay constants as recommended by Steiger and Jäger[44] were used in this study. Individual fusion step uncertainties are quoted excluding the common uncertainty factor in the flux monitor determination. Pooled ages are given as weighted means using the inverse of the variance as a weighting factor. Pooled uncertainties in the ages are quoted at the 1σ level.

Luminescence dating. Luminescence dating methods determine the time of deposition and burial of sediments using grains of quartz and feldspar as natural dosimeters. Owing to exposure to natural ionizing radiation, electrons in the crystal lattice of quartz or feldspar may become excited and trapped at meta-stable energy levels (electron traps). In traps of sufficient stability (thermal trap depth), the trapped charge concentration will increase during burial owing to continued exposure to ionizing radiation. For light-sensitive traps, the trapped charge is liberated when the mineral is exposed to light during sediment erosion, transport and deposition. The trapped-charge concentration in these traps is thus proportional to the time elapsed since the last exposure to light, that is, the last deposition and burial event[47]. For luminescence dating, both the radiation exposure since burial (palaeodose, in Gy) and the yearly radiation exposure (dose rate, in Gy per kyr) need to be determined. The depositional age (in kyr) is then given by: age = palaeodose/dose rate.

Luminescence dating methods are widely applied to date deposits formed during the last glacial cycle (~120 kyr). For this period, the optically stimulated luminescence (OSL) signal of quartz is usually most suitable. However, the saturation of this signal at relatively low doses prohibits its application to older deposits. For deposits beyond the quartz OSL age range, feldspar infrared stimulated luminescence (IRSL) methods provide an alternative. In recent years, reliable feldspar IRSL methods have been developed and tested[48,49]. These post-infrared IRSL (pIRIR) methods circumvent issues with regard to athermal fading of the conventional IRSL signal (anomalous fading; for example[50],) and are often applicable up to ages of 600 kyr (ref. 20). Older sediments may be dated using the quartz thermally transferred OSL signal, but recent studies have shown that the signal is not thermally stable and may yield inaccurate results (reviewed by ref. 51). Methods using the violet stimulated luminescence (VSL) signal of quartz[52,53] may potentially provide an alternative, but these are still in early stages of development.

The cemented sediment infills of four *Pseudodon* shells (DUB9735, DUB9736, DUB1006-e, and the engraved shell DUB1006-fL) were investigated, as well as the sediment infill of a *Stegodon trigonocephalus* skull from the Trinil *Hauptknochenschicht* (DUB4977). From two of these (DUB1006-fL and DUB4977), two samples for luminescence dating were obtained, which results in a total of seven investigated samples. The size of the shell infills was approximately 5 cm × 4 cm × 2 cm. The Stegodon skull infill was much larger (approximately 50 cm × 30 cm × 30 cm), and two cemented pieces of approximately 10 cm × 5 cm × 5 cm were taken from it for dating. The sediment of sample DUB9736 consisted mostly of silty sand with some gravel and shell remains, whereas all other samples consisted largely of sandy silt. In the darkroom laboratory of the Netherlands Centre for Luminescence dating, the outer 1–2 mm of sediment was removed from each of the cemented blocks with a knife (shells) or water-cooled low-speed saw (skull). The outer material was used for dose-rate analysis, whereas the inner portion of the blocks (which had remained unexposed to light since deposition) was used for palaeodose estimation.

For dose-rate estimation, concentrations of uranium, thorium and potassium were measured using neutron activation analysis at the Reactor Institute Delft (TU Delft, The Netherlands). From these concentrations, infinite matrix dose rates were calculated[54], assuming 20% ± 10% ^{222}Rn escape for the ^{238}U decay chain, and 5% ± 3% ^{220}Rn escape for the ^{232}Th decay chain. Effective dose rates were then calculated, taking into account grain size attenuation[55], water content[56], and for the feldspar samples a contribution from internal potassium (^{40}K) and rubidium (^{87}Rb)[57,58]. The contribution from cosmic rays was also included, assuming gradual burial to a depth of 12 m below the surface and taking into account the geographic position of the site[59].

Several assumptions had to be made in estimating the dose rate, as we had little material for analysis, and information on the original context of the shells was limited. For each of these assumptions, we estimated reasonable uncertainties that were incorporated into the overall dose-rate uncertainty and subsequently in the reported ages. Here, we discuss the most important assumptions and the associated uncertainties with regard to the dose-rate analysis. The largest source of uncertainty is the average water content of the sediment during the period of burial. On the basis of the lithology of the sample, we assumed a water content of 50% ± 25% by weight for the samples consisting of sandy silt (DUB9735, DUB1006-e, DUB1006-fL, DUB4977), and 20% ± 10% for the sample consisting of silty sand (DUB9736). The uncertainties were chosen to encompass a wide range of possible water contents as well as variations in water content over burial time.

With regard to the gamma dose rate, we had to make two additional assumptions. First, we assume that the sediments surrounding the shells are similar to the sediment infill. This assumption is based on remnants of sediment found on the outer shell surface, but cannot be verified for the entire sphere from which the gamma dose originates (~25 cm around the shell). In the absence of better information, we propose that the effect of heterogeneity of the deposits may be reflected by differences in the gamma dose rates obtained for the seven samples, which show a relative standard deviation of 11% (see Supplementary Table 6). Second, we assume that the samples are surrounded by sediment only, thereby ignoring the influence of the shell itself, as well as other shells that may have been present in the direct vicinity. Although it has been established that shells may influence the dose rate and the dose-rate heterogeneity[60], the shells at the Trinil site are thin-walled and their influence on dose rates will be minor (estimated to be <5%). The combined effect of these uncertainties (12%) is incorporated as an additional relative uncertainty for the gamma dose rate estimates.

Both quartz and feldspar minerals were prepared for palaeodose estimation. Samples were brittle and crushed by hand after removal of the light-exposed outer parts. The grains were treated with HCl and H_2O_2 to remove carbonates and organics, and then wet-sieved to obtain a relatively narrow grain size for analysis. The exact grain size fraction prepared for analysis differs between samples (see Supplementary Table 6) owing to slight lithological differences and variations in the amount of material that was available. The obtained fractions were density separated in a sodium heteropolytungstate solution (LST) fastfloat at 2.58 kg dm^{-3}; the light fraction consisted largely of K-rich feldspar and all samples were lightly etched with 10% HF for 15 min to remove the surface layer of the grains that is exposed to external alpha particles during geological burial. Quartz minerals were obtained from the heavy fraction through treatment with 40% HF for 40 min.

Preliminary investigations showed that conventional quartz OSL methods[61] could not be used for dating because the signals showed an extremely dim fast component, and had reached saturation. Also VSL signals (following ref. 53) showed unwanted behaviour (for example, dim signals, no initial fast decay). We therefore abandoned quartz OSL and VSL dating at this stage, and concentrated on feldspar methods.

Feldspar equivalent dose determination used the feldspar pIRIR single-aliquot regenerative dose (SAR) method[20]. The pIRIR measurements were made for 100 s at 290 °C, and were preceded by a heating for 60 s at 320 °C and infrared exposure at 50 °C for 100 s. At the end of each SAR cycle, samples were exposed to infrared light at 330 °C for 40 s to fully reset the pIRIR signal. Standard rejection criteria within the SAR protocol were applied, with results being accepted if recycling was within 15% from unity and the uncertainty on the test dose was lower than 15%.

The pIRIR luminescence sensitivity of the Stegodon samples (DUB4977) proved to be poor, resulting in rejection of all measured aliquots and analysis of these two samples had to be abandoned. For each of the remaining five samples luminescence signals were sufficient (see Extended Data Fig. 9e for examples): between 6 and 19 single aliquots yielded equivalent doses after applying the rejection criteria. Dose–response curves were all similar and could be fitted with a single saturating exponential plus a linear component given by $L(D) = A[1 - \exp(-D/D_0)] + BD$, where L is the sensitivity-corrected luminescence signal as a function of the absorbed dose D (in Gy), A and B are constants and D_0 (in Gy) is a parameter indicating the onset of saturation of the exponential component. Murray and Wintle[61] have suggested that the reliable equivalent dose estimation is possible for the dose range up to $2D_0$. We adopted this criterion to assess the validity of the equivalent dose estimates, as the suitability of the linear component for dating has not been established[62]. For all investigated samples, at least half of the aliquots returned equivalent doses above the $2D_0$ limit, as illustrated in Extended Data Fig. 9e for samples DUB1006-f(I) and (II) from the engraved shell. From this, we infer that the sample equivalent dose must be greater than the $2D_0$ value, that is, the sample-average saturation limit ($2D_0$) provides a minimum equivalent dose estimate (Table 1).

As only minimum equivalent doses can be obtained, we can only provide minimum age estimates based on the luminescence dating analysis. However, we should consider that these minimum ages might be affected by incomplete resetting of the pIRIR signal at the time of deposition. pIRIR remnant doses for modern deposits may range from less than 10 Gy for aeolian and beach samples[20] up to 55 Gy for glacial outwash deposits[21]. For the Trinil *Hauptknochenschicht* deposits (Supplementary Information sections 1 and 2), we assume a residual dose of 30 ± 15 Gy at the time of deposition, where the 2σ range encompasses all reported literature remnant dose values for modern samples. We subtract this residual dose from the minimum equivalent dose to obtain an estimate of the minimum palaeodose (that is, the dose absorbed since the time of deposition and burial). As all samples are from similar depositional environments, the uncertainty on this estimate is regarded as a systematic error shared by the samples.

By combining the minimum palaeodose and dose rate for each sample, minimum ages are obtained for the cemented sediment infill of the investigated shells from the *Hauptknochenschicht*. As all samples are from the same stratigraphic layer (the Trinil *Hauptknochenschicht*), the oldest result could be interpreted as the minimum age for these deposits. However, given that all samples return similar results, we prefer a more conservative and robust approach based on an average of all samples, taking into account their shared uncertainties (systematic uncertainty ~10%).

22. Benthem Jutting, T. v. Non marine Mollusca from fossil horizons in Java with special reference to the Trinil fauna. *Zoologische Mededelingen* **20,** 83–180 (1937).
23. Jongerius, A. & Heintzberger, G. *The Preparation of Mammoth-sized Thin Sections* (Netherlands Soil Survey Institute, 1963).
24. Benyarku, C. A. & Stoops, G. *Guidelines for Preparation of Rock and Soil Thin Sections and Polished Sections* Vol. 33 (Universitat de Lleida, 2005).
25. Stoops, G. *Guidelines for Analysis and Description of Soil and Regolith Thin Sections* (Soil Science Society of America, 2003).
26. Pascal, L. *Catalogue des Mollusques Terrestres et des Eaux Douces du Département de la Haute-Loire et des Environs de Paris* (Imprimerie Nationale, 1873).
27. Spoor, C. F., Zonneveld, F. W. & Macho, G. A. Linear measurements of cortical bone and dental enamel by computed tomography: applications and problems. *Am. J. Phys. Anthropol.* **91,** 469–484 (1993).
28. Dutailly, B., Coqueugniot, H., Desbarats, P., Gueorguieva, S. & Synave, R. in *IEEE International Conference on Image Processing (ICIP09)* 2505–2508 (IEEE, 2009).
29. Claassen, C. *Shells* (Cambridge Univ. Press, 1998).
30. Nielsen, A. E. Trampling the archaeological record: an experimental study. *Am. Antiq.* **56,** 483–503 (1991).
31. Bender Kotzian, C. & Simões, M. G. Taphonomy of recent freshwater molluscan death assemblages, Touro Passo Stream, Southern Brazil. *Rev. Brasil. Paleontol.* **9,** 243–260 (2006).
32. d'Errico, F., Jardon-Giner, P. & Soler Major, B. in *Traces et Fonction: Les Gestes Retrouvés* Vol. 50 (eds Anderson, P. C., Beyries, S., Otte, M. & Plisson, H.) 243–254 (Editions ERAUL, 1993).
33. Toth, N. & Woods, M. Molluscan shell knives and experimental cut-marks on bones. *J. Field Archaeol.* **16,** 250–255 (1989).
34. Cristiani, E., Lemorini, C., Martini, F. & Sarti, L. in *From Hooves to Horns, from Mollusc to Mammoth: Manufacture and Use of Bone Artefacts from Prehistoric Times to the Present. Proc. 4th Meet. ICAZ Worked Bone Research Group (Tallinn, 26–31 August 2003)* Vol. 15 (eds Luik, H., Choyke, A. M., Batey, C. & Lougas, L.) 319–324 (Muinasaja Teadus series, Tallinn Book Printers, 2005).
35. Tumung, L., Bazgir, B., Ahmadi, K. & Shadmehr, A. Understanding the use-wears on non-retouched shells *Mytilus galloprovincialis* and *Ruditapes decussatus* by performing wood working experiment: an experimental approach. *IOP Conf. Ser. Materials Science and Engineering* **37,** 1–10 (2012).
36. Cuenca Solana, D., Clemente Conte, I. & Gutiérrez Zugasti, I. Utilización de instrumentos de concha durante el Mesolítico y Neolítico inicial en contextos litorales de la región cantábrica: programa experimental para el análisis de huellas de uso en materiales malacológicos. *Trabajos Prehistoria* **67,** 211–225 (2010).
37. Bello, S. M. & Soligo, C. A new method for the quantitative analysis of cutmark micromorphology. *J. Archaeol. Sci.* **35,** 1542–1552 (2008).
38. d'Errico, F. *L'Art Gravé Azilien. De la Technique à la Signification* (CNRS, 1995).
39. Fritz, C. *La Gravure dans l'Art Mobilier Magdalénien, du Geste à la Représentation: Contribution de l'Analyse Microscopique* Vol. 75 (Maison des Sciences de l'Homme, 1999).
40. Henshilwood, C. S. & d'Errico, F. in *Homo Symbolicus: The Dawn of Language, Imagination and Spirituality* (eds Henshilwood, C. S. & d'Errico, F.) 75–96 (Benjamins, 2011).
41. Texier, P. J. *et al.* A Howiesons Poort tradition of engraving ostrich eggshell containers dated to 60,000 years ago at Diepkloof Rock Shelter, South Africa. *Proc. Natl Acad. Sci. USA* **107,** 6180–6185 (2010).
42. Peng, F. *et al.* An engraved artifact from Shuidonggou, an early Late Paleolithic site in Northwest China. *Chin. Sci. Bull.* **57,** 4594–4599 (2012).
43. Kuiper, K. F. *et al.* Synchronizing rock clocks of Earth history. *Science* **320,** 500–504 (2008).
44. Steiger, R. H. & Jager, E. Subcommission on geochronology: convention on the use of decay constants in geo- and cosmochronology. *Earth Planet. Sci. Lett.* **36,** 359–362 (1977).
45. Lee, J.-Y. *et al.* A redetermination of the isotopic abundances of atmospheric Ar. *Geochim. Cosmochim. Acta* **70,** 4507–4512 (2006).
46. Koppers, A. A. P. ArArCalc—software for $^{40}Ar/^{39}Ar$ age calculations. *Comput. Geosci.* **28,** 605–619 (2002).
47. Preusser, F. *et al.* Luminescence dating: basics, methods and applications. *Quat. Sci. J.* **57,** 95–149 (2008).
48. Thomsen, K. J., Murray, A. S., Jain, M. & Bøtter-Jensen, L. Laboratory fading rates of various luminescence signals from feldspar-rich sediment extracts. *Radiat. Meas.* **43,** 1474–1486 (2008).
49. Kars, R. H., Busschers, F. S. & Wallinga, J. Validating post IR-IRSL dating on K-feldspars through comparison with quartz OSL ages. *Quat. Geochronol.* **12,** 74–86 (2012).
50. Wallinga, J., Bos, A. J. J., Dorenbos, P., Murray, A. S. & Schokker, J. A test case for anomalous fading correction in IRSL dating. *Quat. Geochronol.* **2,** 216–221 (2007).
51. Duller, G. A. T. & Wintle, A. G. A review of the thermally transferred optically stimulated luminescence signal from quartz for dating sediments. *Quat. Geochronol.* **7,** 6–20 (2012).
52. Jain, M. Extending the dose range: Probing deep traps in quartz with 3.06 eV photons. *Radiat. Meas.* **44,** 445–452 (2009).
53. Ankjærgaard, C., Jain, M. & Wallinga, J. Towards dating Quaternary sediments using the quartz Violet Stimulated Luminescence (VSL) signal. *Quat. Geochronol.* **18,** 99–109 (2013).
54. Guérin, G., Mercier, N. & Adamiec, G. Dose-rate conversion factors: update. *Ancient TL* **29,** 5–8 (2011).
55. Mejdahl, V. Thermoluminescence dating: beta-dose attenuation in quartz grains. *Archaeometry* **21,** 61–72 (1979).
56. Aitken, M. J. *Thermoluminescence Dating* (Academic Press, 1985).
57. Huntley, D. J. & Baril, M. R. The K content of the K-feldspars being measured in optical dating or in thermoluminescence dating. *Ancient TL* **15,** 11–13 (1997).
58. Huntley, D. J. & Hancock, R. G. V. The Rb contents of the K-feldspar grains being measured in optical dating. *Ancient TL* **19,** 43–46 (2001).
59. Prescott, J. R. & Hutton, J. T. Cosmic ray contributions to dose rates for luminescence and ESR dating: large depths and long-term time variations. *Radiat. Meas.* **23,** 497–500 (1994).
60. Cunningham, A. C. *et al.* Extracting storm-surge data from coastal dunes for improved assessment of flood risk. *Geology* **39,** 1063–1066 (2011).
61. Murray, A. S. & Wintle, A. G. The single aliquot regenerative dose protocol: potential for improvements in reliability. *Radiat. Meas.* **37,** 377–381 (2003).
62. Murray, A. S., Buylaert, J. P., Henriksen, M., Svendsen, J. I. & Mangerud, J. A review of quartz optically stimulated luminescence characteristics and their relevance in single-aliquot regeneration dating protocols. *Radiat. Meas.* **43,** 776–780 (2008).

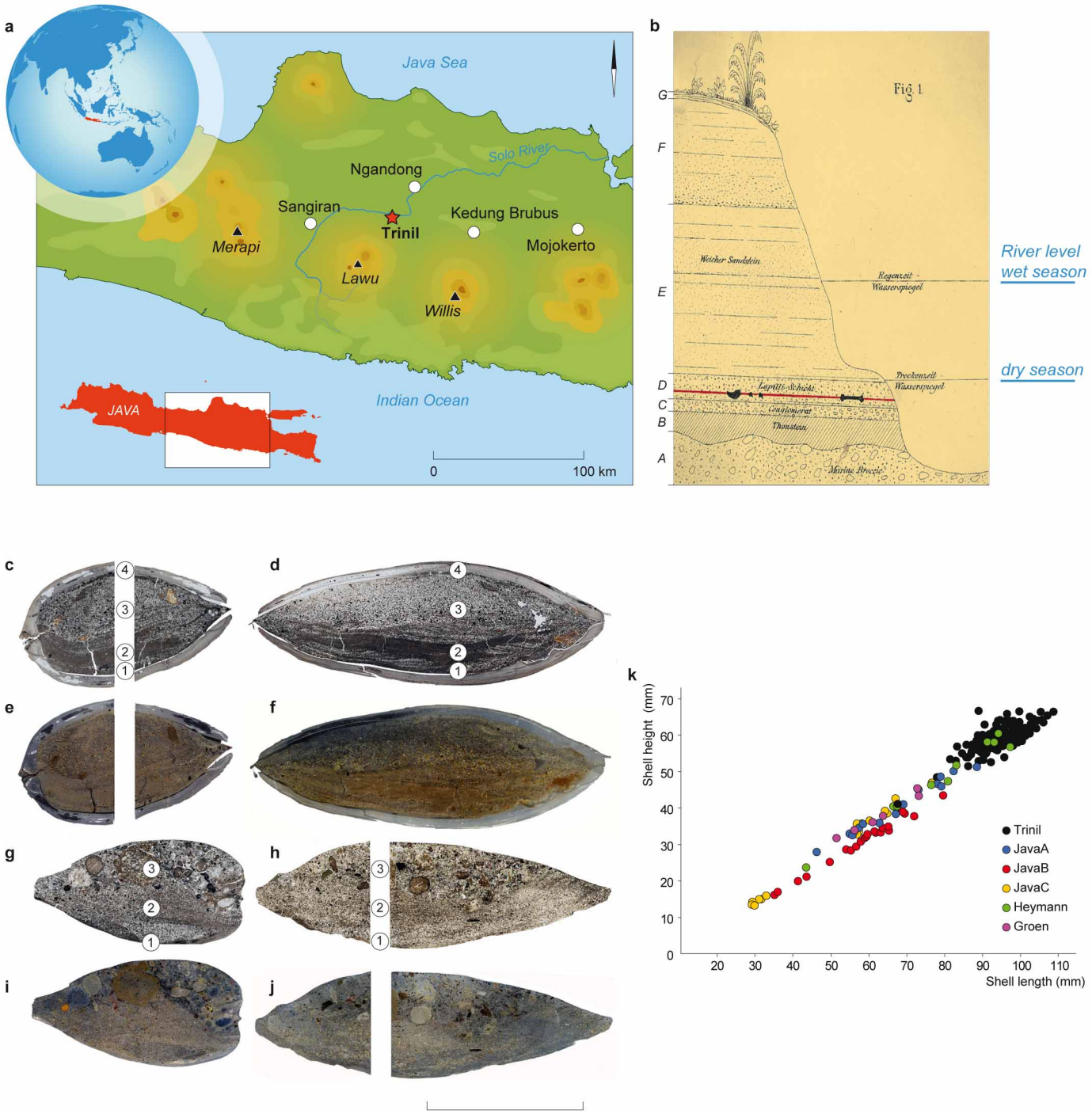

Extended Data Figure 1 | The *Pseudodon* shells from Trinil. (See Supplementary Information sections 1-2 and 4). **a**, Map of Central Java with major hominin sites and volcanic uplands. **b**, Stratigraphy of Trinil. A = Marine breccia ("Marine Breccie"). B = Mudstone ("Thonstein"). C = Conglomerate ("Conglomerat"). D = Trinil *Hauptknochenschicht* ("Lapilli Schicht") containing *H. erectus* fossils. E = Soft sandstone ("Weicher Sandstein"). *F* = unnamed level. G = soil. **c**–**j**, Scans of thin sections of fossil *Pseudodon* infilled shell DUB 9717-b (**c**–**f**) and of infill DUB 9735 (**g**–**j**). The numbers refer to the numbered descriptions in Supplementary Information section 2. Images **c**, **d**, **g** and **h** are made by reflective scanning; images **e**, **f**, **i**, **j** are made by transmissive scanning. Scale bar, 4 cm. **k**, *Pseudodon* shell length–height data. Black dots show the fossil *Pseudodon vondembuschianus trinilensis* assemblage from Trinil. Coloured dots show recent *Pseudodon vondembuschianus* assemblages collected on Java in the 1930s.

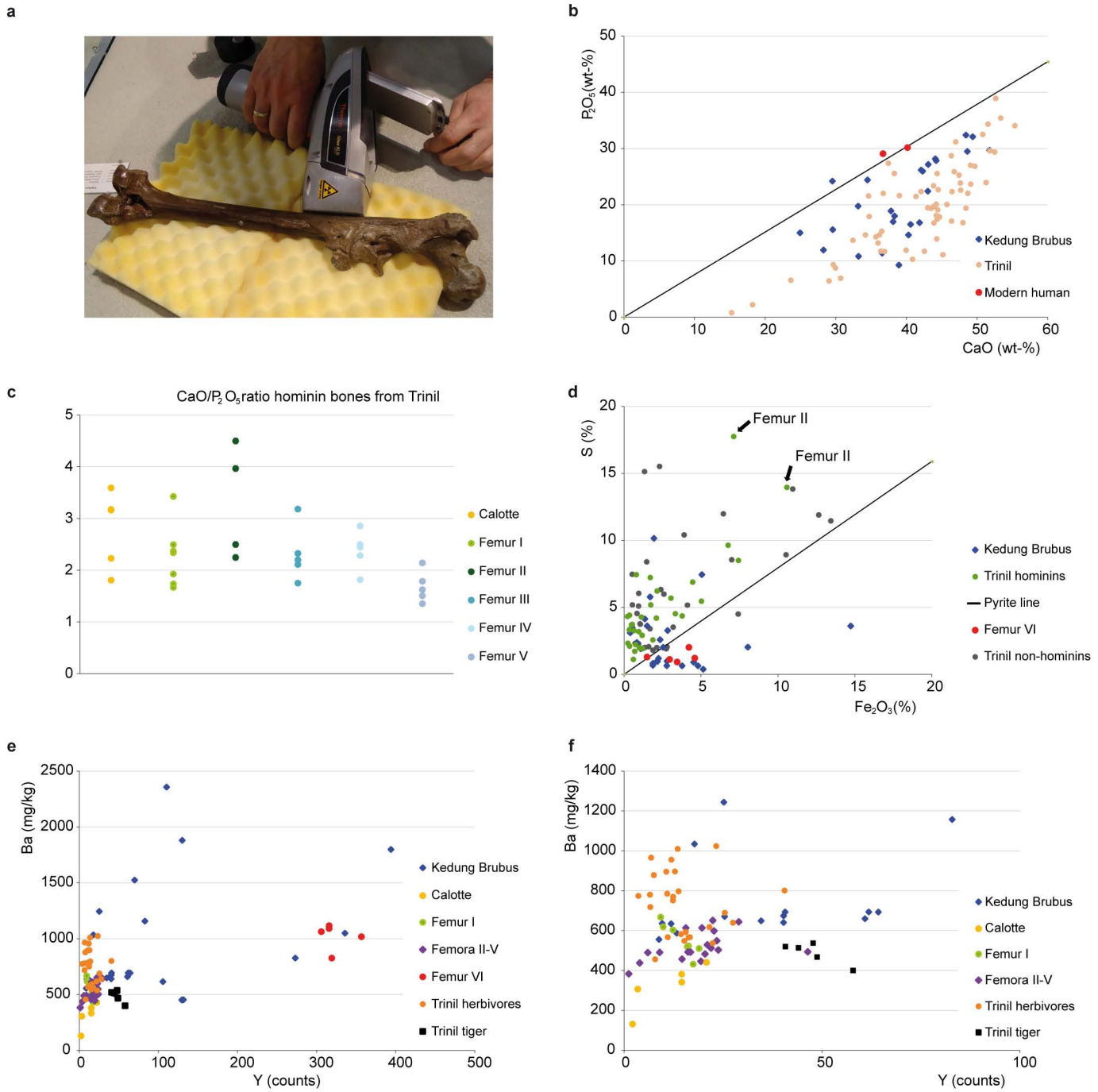

Extended Data Figure 2 | XRF analysis. (See Supplementary Information section 3 and Supplementary Table 2.) **a**, Fossil Femur I from Trinil undergoing XRF analysis. Dorsomedially, just below mid-shaft is a small white circle representing the filled hole where K. P. Oakley drilled a bone sample. **b**, Scatter plot of CaO versus P_2O_5. All values measured with hand-held XRF on hominin and non-hominin bones are included. The line represents the CaO/P_2O_5 ratio in fresh bone. **c**, CaO/P_2O_5 ratios of hominin bones from Trinil. The values were measured with hand-held XRF at four to seven locations on the bones. 'Calotte' indicates the skull cap named Trinil 2. **d**, Scatterplot of sulphur (S) versus Fe_2O_3 content of fossil bones. Data points represent all measurements performed on hominin fossils from Trinil, plus non-hominin fossil fauna from Trinil and Kedung Brubus. In pyrite, the Fe_2O_3/S ratio is 1.126. The arrows highlight the measurement locations on Femur II where elevated contents of S and Fe_2O_3 were measured, which explains the two high CaO/P_2O_5 values (4 and 4.5) in **c**. **e**, Scatterplot of Ba versus Y (calcium-corrected) content of fossil bones. Data points represent all measurements done on hominin fossils from Trinil, plus non-hominin fauna from Trinil and Kedung Brubus. **f**, Detail of the Ba–Y scatterplot in **e**.

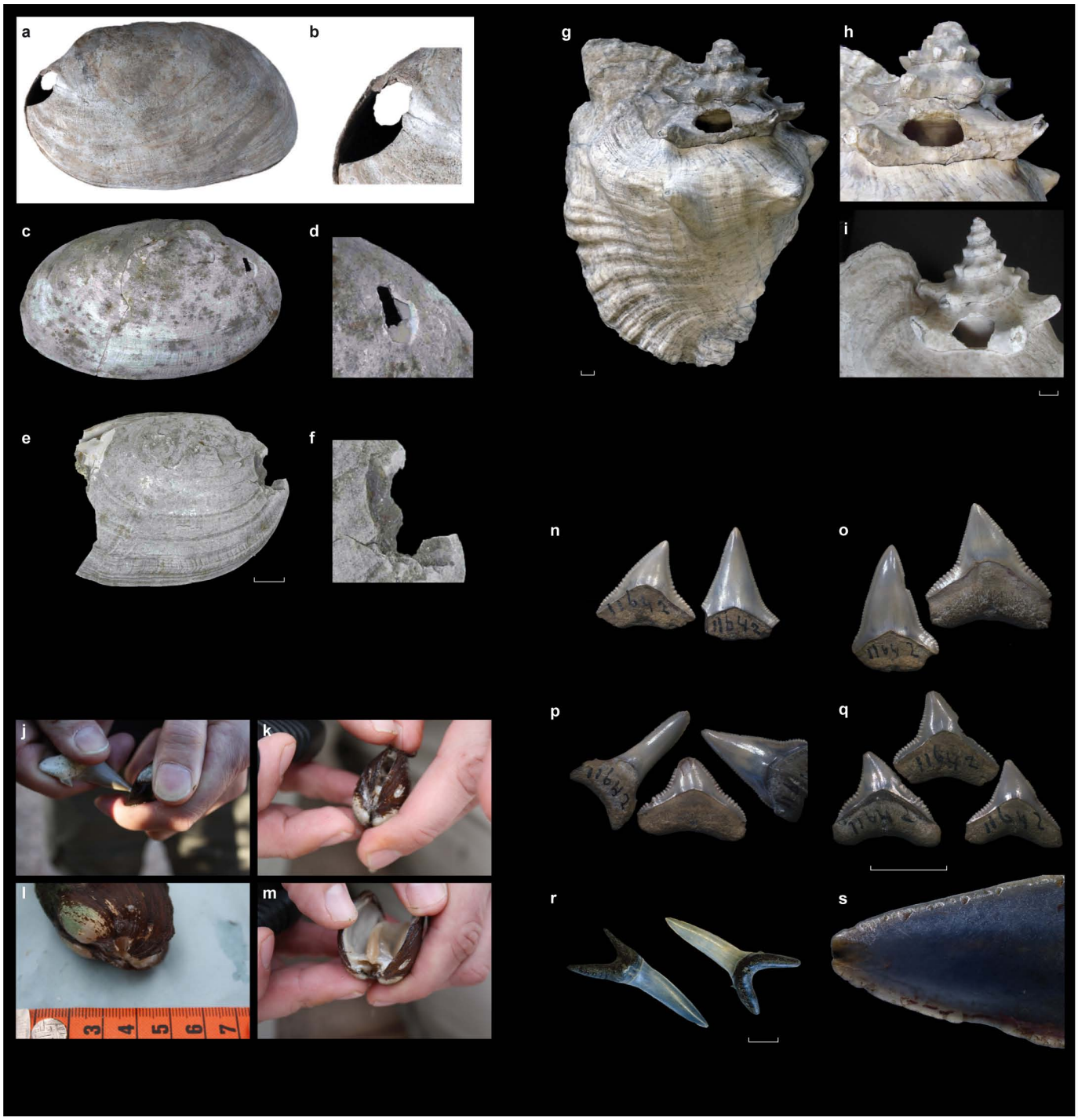

Extended Data Figure 3 | Holes in shells. (See Supplementary Information sections 5–7.) **a**, Fossil *Pseudodon* shell DUB9718-a (detail in **b**); **c**, DUB5234-aR (detail in **d**); **e**, DUB9714-bR (detail in **f**). Scale bar, 1 cm. **g**, Recent *Lobatus gigas* ("Strombus") shell with a hole at the location of the columellar muscle attachment, made by pre-Hispanic modern humans (photograph provided by C. L. Hofman). Scale bar, 1 cm. **h**, Detailed view of **g**. **i**, Similar hole in another *Lobatus gigas* specimen (photograph provided by A. Antczak). Scale bar, 1 cm. **j**, Experimentally drilling a hole in a living *Potamida littoralis* specimen, using a fossil shark tooth. **k**, Hole drilled, damaging the adductor muscle. **l**, The shell starts to gape. **m**, The valves can be easily opened. **n**, Example of undamaged fossil teeth of the shark species *Glyphis* sp. from Trinil. **o**, *Glyphis* teeth with side damage, on the serrated edge. **p**, *Glyphis* sp. teeth with tip damage. **q**, *Glyphis* sp. teeth with tip and side damage. Scale bar, in **q**, 1 cm, also applies to **n**–**p**. **r**, Fossil teeth of the shark species *Carcharius taurus* from Trinil. Scale bar, 1cm. **s**, Detail of a fossil *Carcharius taurus* tooth.

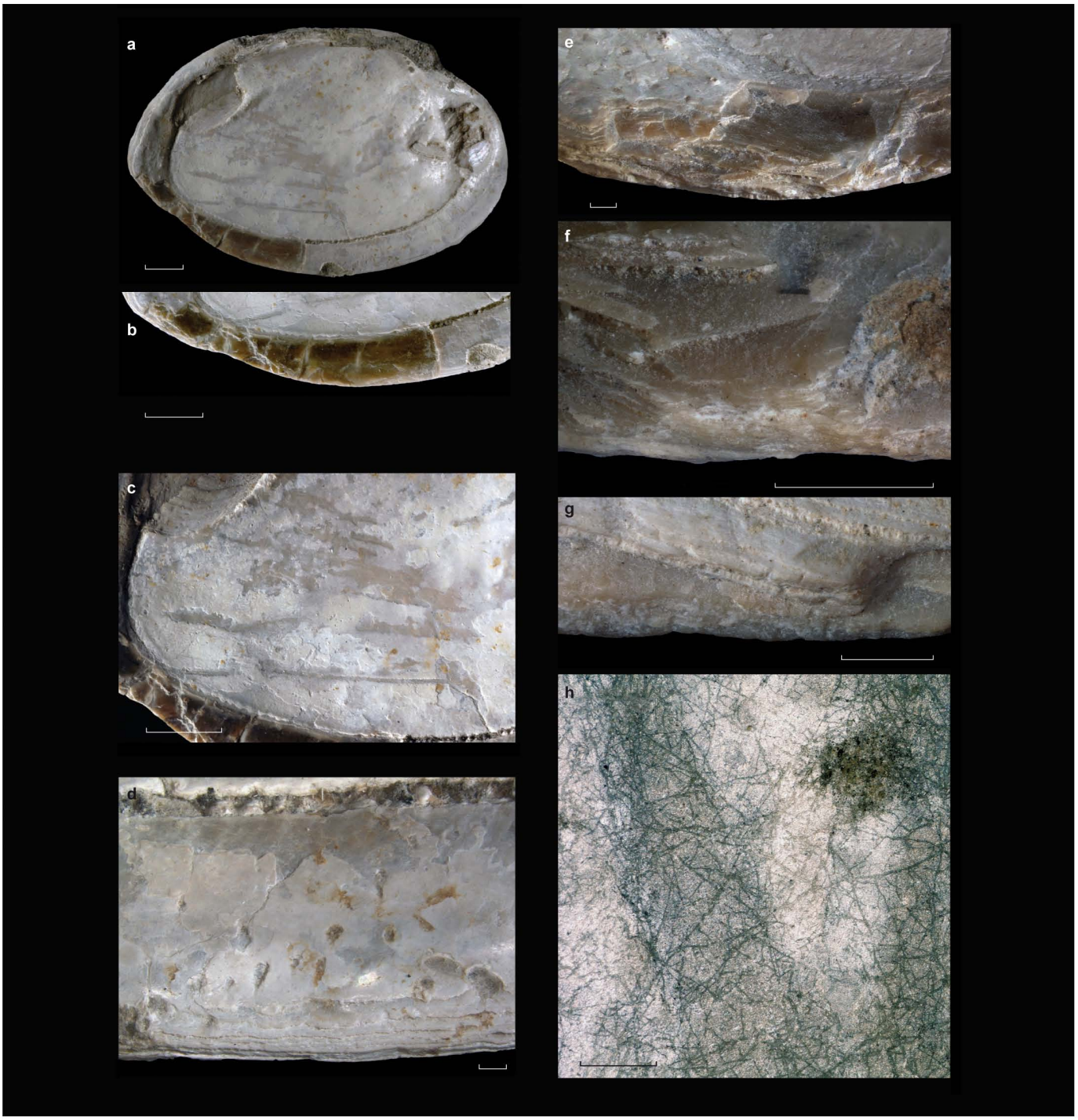

Extended Data Figure 4 | Shell modification on *Pseudodon* shell DUB5234-dL. (See Supplementary Information section 8.) **a**, Interior of the shell valve. **b**, Ventral margin with contiguous flake scars. **c**, Shallow striations parallel to the retouched edge. **d**, Micropits made by pecking with a sharp agent. **e**–**g**, Magnifications of the retouched edge, showing step fractures associated with rounding and smoothing of the edge. **h**, Traces of damage by roots or fungi inside and across the striations. Scale bars: 1 cm in **a** and **b** and **f**, 1.25 mm in **c**, 1.5 mm in **d**, 0.5 mm in **e** and **h**, and 1 mm in **g**.

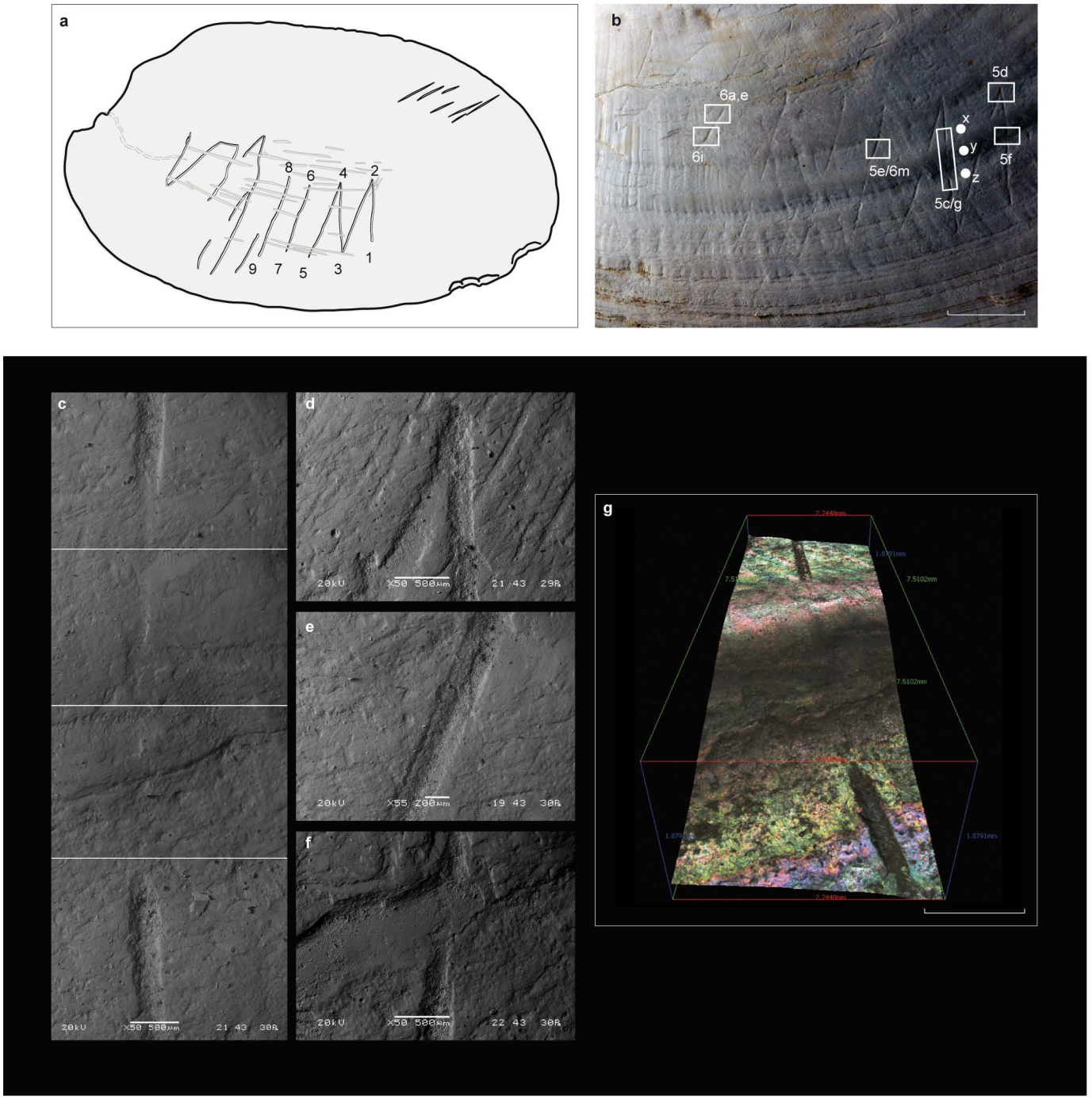

Extended Data Figure 5 | Engraved pattern on *Pseudodon* shell DUB1006-fL. (See Supplementary Information section 9.) **a**, Tracing of the engraved lines, with numbers indicating the sequence of engraving. **b**, White rectangles refer to the locations of the images shown in the panels of Extended Data Figs 5 and 6, featuring portions of grooves and intersections. The white dots indicate the location of the areas where three-dimensional roughness parameters were measured (Supplementary Table 4). Scale bar, 1 cm. **c**, Composite of four SEM images made of a portion of groove number 3–4; numbered locations of the grooves on the shell are shown in panels **a** and **b**. **d**, Intersection number 2. **e**, Portion of groove number 6–7. **f**, Portion of groove number 1–2. **g**, Infinite Focus image of a portion of groove number 3–4; see **b** for location on the shell (same as the location of **c**). Scale bar, 1 mm.

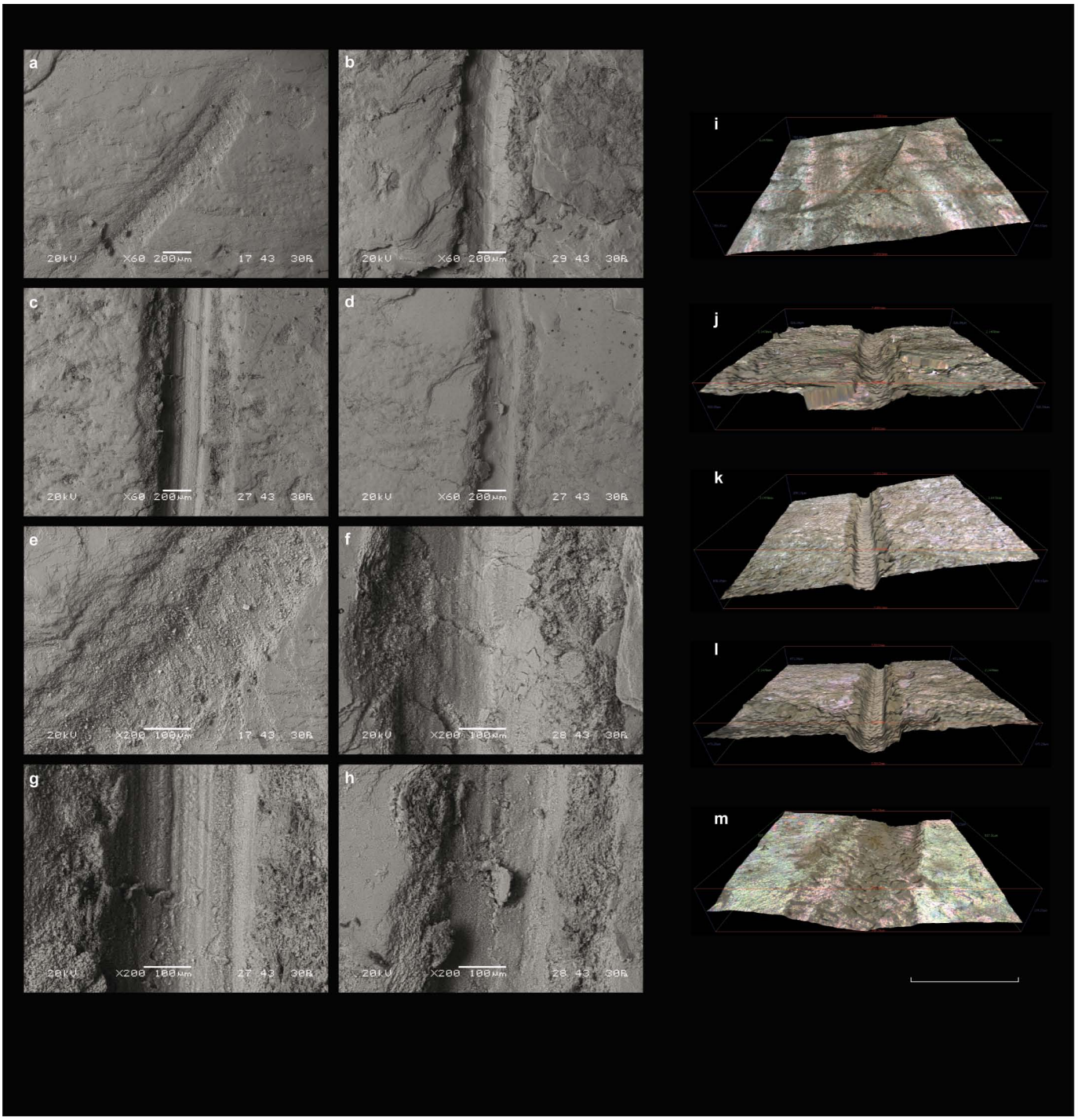

Extended Data Figure 6 | Comparison of engraving on DUB1006-fL with experimental engravings. (See Supplementary Information section 9.) **a**, Portion of groove in DUB1006-fL (see Extended Data Fig. 5b for location on the shell). **b**, Experimental groove made with shark tooth tip. **c**, Experimental groove made with flint point. **d**, Experimental groove made with steel scalpel. **e**–**h**, Higher magnification (200× instead of 60×) of Extended Data Fig. 5a–d. **i**, Infinite Focus image of groove in DUB1006-fL (see Extended Data Fig. 5b for location on the shell). **j**, Infinite Focus image of experimental groove made with shark tooth tip. **k**, Infinite Focus image of experimental groove made with flint point. **l**, Infinite Focus image of experimental groove made with steel scalpel. **m**, Infinite Focus image of groove number 6–7 in DUB1006-fL (see Extended Data Fig. 5b for location on the shell). Scale bar, 1 mm.

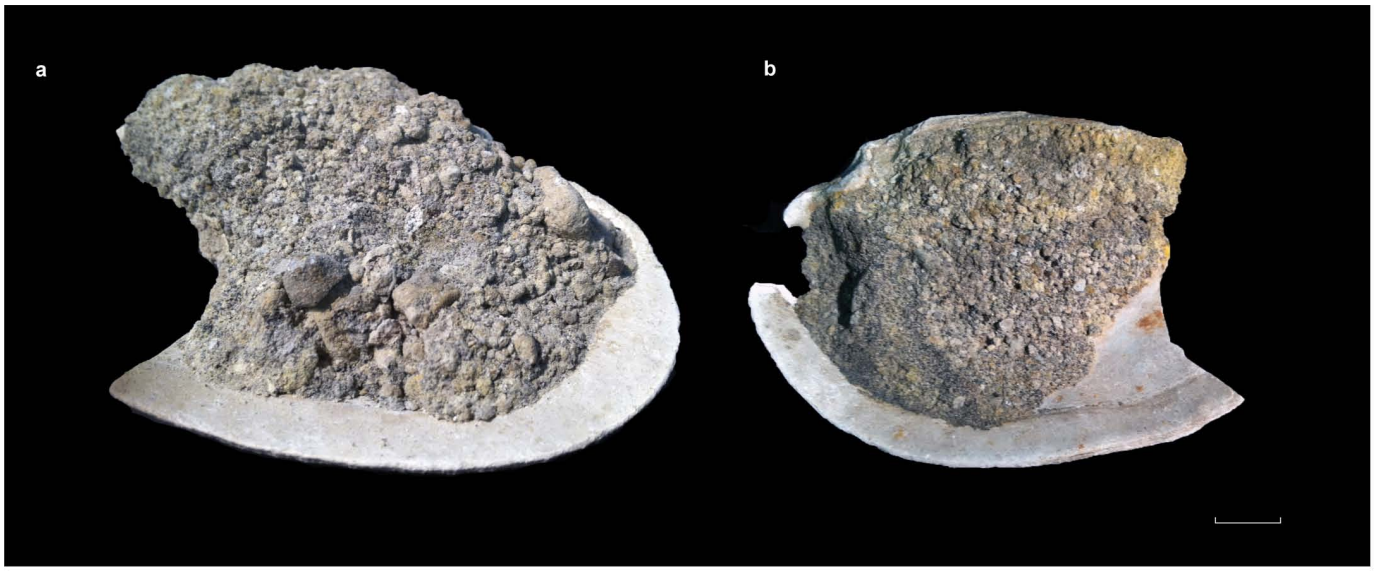

c

Sample ID	Young Age (ma)	1σ (Ma)	Middle Age (ma)	1σ (Ma)	Old Age (ma)	1σ (Ma)
Loose sediment			1.18	0.06	1.47	0.06
(Trinil-1)			1.19	0.06	1.52	0.16
					1.69	0.08
					1.72	0.08
					1.74	0.08
					1.74	0.09
DUB9721-bR	0.33	0.10	1.11	0.12	1.43	0.14
(Trinil-2)	0.56	0.13	1.11	0.11	1.73	0.16
	0.70	0.09	1.24	0.21		
	0.75	0.12				
	0.81	*0.17*	*0.81*	*0.17*		
DUB9714-bR	0.47	0.14	1.19	0.16	1.69	0.10
(Trinil-3)	0.55	0.49			1.89	0.15
	0.63	0.12				
	0.73	0.22				
	0.81	*0.12*	*0.81*	*0.12*		
	0.95	*0.16*	*0.95*	*0.16*		

Extended Data Figure 7 | $^{40}Ar/^{39}Ar$ analysis. (See Supplementary Information section 10.) **a**, **b**, *Pseudodon* shells DUB9721-bR (Trinil-2) and DUB9714-bR (Trinil-3) with detrital infilling used for $^{40}Ar/^{39}Ar$ analysis. The other side of hominin-modified valve DUB9714-bR is featured in Extended Data Fig. 3e. Scale bar, 1 cm. **c**, $^{40}Ar/^{39}Ar$ analysis results on multiple-grain hornblende obtained from three samples. They constitute three populations (age groups) of 'young', 'middle' and 'old' age respectively. Note that three individual analyses (indicated in italics) belong to both the 'young' and 'middle' populations on statistical grounds.

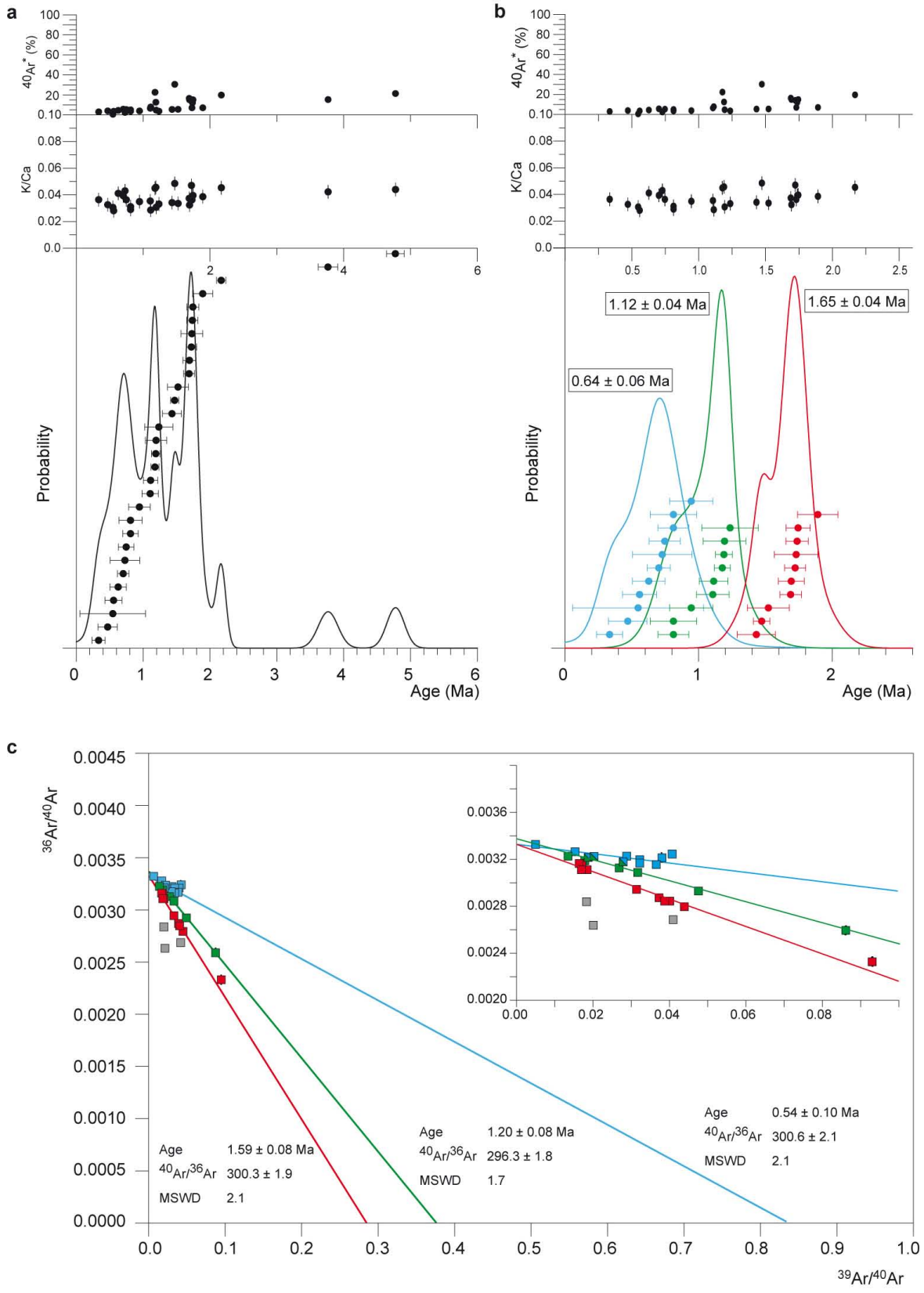

Extended Data Figure 8 | $^{40}Ar/^{39}Ar$ results. (See Supplementary Information section 10.) **a**, Total population of hornblende data, showing probability density curve, individual analyses with 1σ analytical uncertainties, and percentage enrichment in radiogenic ^{40}Ar and estimates of the K/Ca ratios calculated from $^{39}Ar/^{37}Ar$ ratios. **b**, Three populations (age groups) as identified in the Trinil sample. Note that three individual analyses belong both to the 'young' (blue) and 'middle' (green) populations on statistical grounds. The error bars represent the 1σ analytical uncertainties. **c**, Inverse isochron representation of all three data sets showing overlap of the respective non-radiogenic intercepts with atmospheric $^{40}Ar/^{36}Ar$ ratios, and the isochron regression of the three subsets in blue (young), green (middle) and red (old) populations. The outliers are in grey. The 1σ error ellipses are in most cases smaller than the symbol size. MSWD, mean squared weighted deviate.

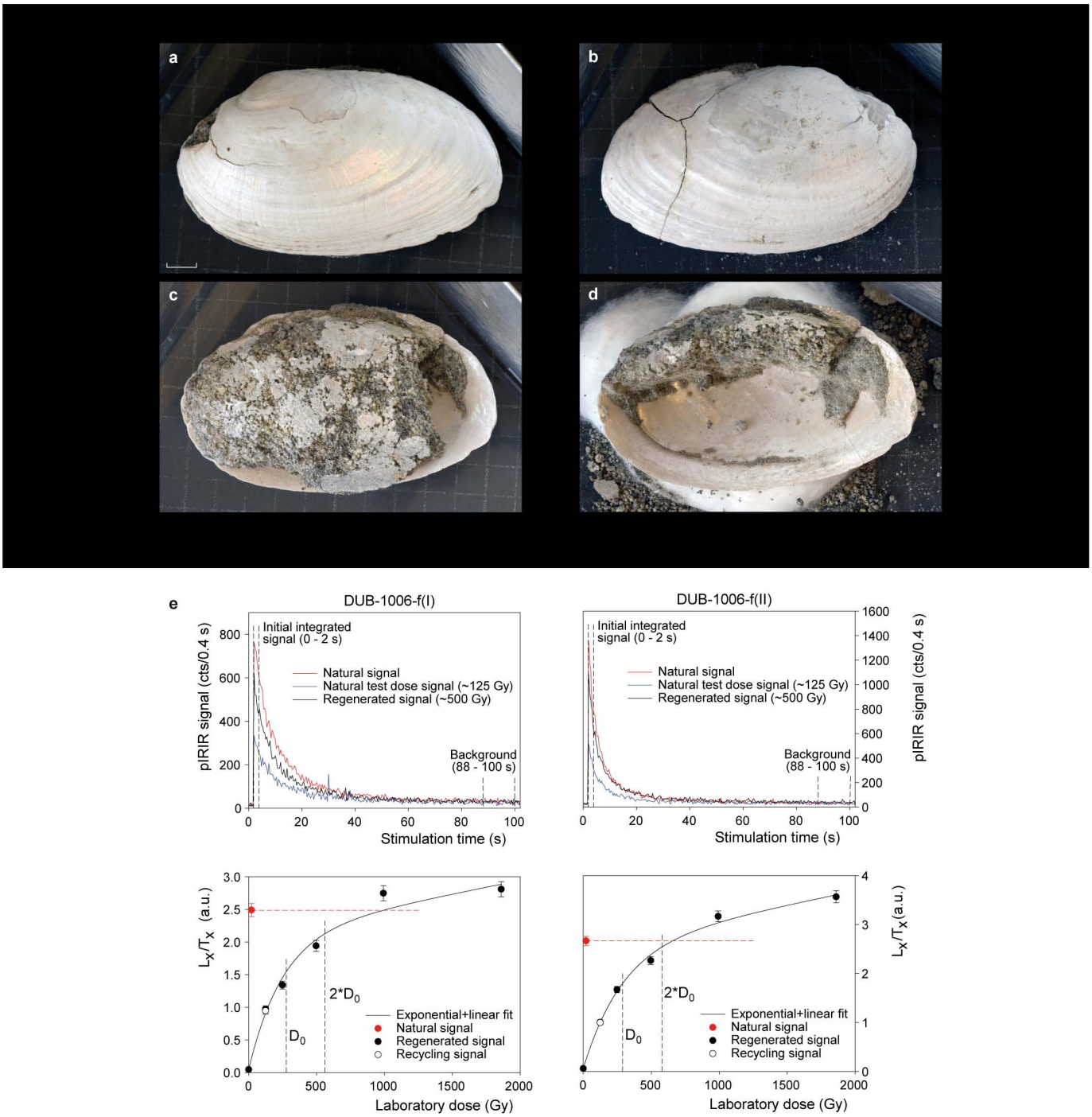

Extended Data Figure 9 | Luminescence dating. (See Supplementary Information section 11.) **a**, Outside of the left valve of *Pseudodon* DUB1006-fL with engraving. **b**, Outside of the right valve. **c**, Inside of the right valve with infill, before sampling for luminescence dating. **d**, Inside of the right valve with infill, after sampling. **e**, pIRIR decay curves and dose–response behaviour for two representative individual aliquots of samples DUB1006-f(I) (left) and (II) (right) obtained from the engraved shell. The upper panels of **e** show the pIRIR signals for the natural dose (L_n), test dose (T_x) and regenerative dose (L_x). Indicated on the graphs are the integration intervals used for analysis. The lower panels of **e** show sensitivity-corrected dose–response curves showing the saturation behaviour, and the natural signal intercept that is above $2D_0$ for both aliquots.

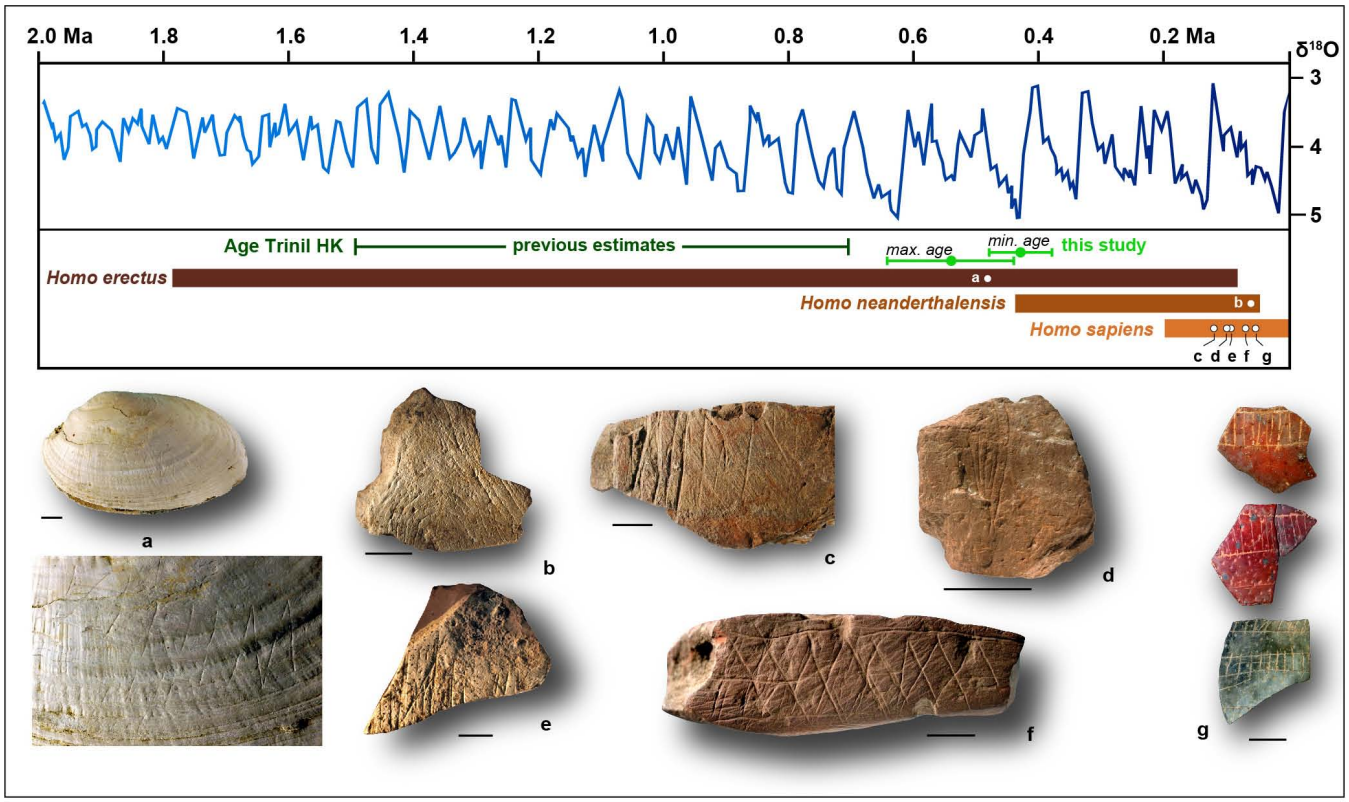

Extended Data Figure 10 | The Trinil engraving in broader archaeological context. (See Supplementary Information section 12.) The upper panel shows dating results from this study compared with previous age estimates, against the background of the marine isotope record. The lower panel shows a selection of engraved objects of Middle and Late Pleistocene age, with the chronological position of each indicated. **a**, Trinil, **b**, Quneitra, **c**, Klasies River Cave 1, **d**, Blombos Cave (~100 kyr), **e**, Qafzeh, **f**, Blombos Cave (~75 kyr), **g**, Diepkloof. Scale bar, 1 cm.